Polymeric Photonic Crystal Fibers for Textile Tracing and Sorting

Brian Iezzi, Austin Coon, Lauren Cantley, Bradford Perkins, Erin Doran, Tairan Wang, Mordechai Rothschild, and Max Shtein

Circular supply chains require more accurate product labeling and traceability. In the apparel industry, product life cycle management is hampered in part by inaccurate, poorly readable, and detachable standard care labels. Instead, this article seeks to enable a labeling system capable of being integrated into the fabric itself, intrinsically recyclable, low-cost, encodes information, and allows rapid readout after years of normal use. In this work, all-polymer photonic crystals are designed and then fabricated by thermal drawing with >100 layers having sub-micrometer individual thickness and low refractive index contrast ($\Delta n = 0.1$). The fibers exhibit reflectance features in the 1–5.5 μm wavelength range, characterized using insitu Fourier transform infrared spectroscopy. Drawn photonic fibers are then woven into fabrics, characterized by near-infrared spectroscopy and short-wave infrared imaging, techniques commonly used in industrial facilities for sorting materials. The fibers' optical design also enables the use of overtone peaks to avoid overlap with parasitic molecular absorption, substantially improving the signal-to-noise ratio (and therefore ease and speed) of readout. The ability to produce kilometers of fiber that are compatible with existing textile manufacturing processes, coupled with low input material cost, make these a potential market-viable improvement over the standard care label.

1. Introduction

Modern consumers increasingly want to know more about the environmental and geopolitical impact of their purchases including how a product is made, what materials go into its manufacture, where it was made, by whom, and under what conditions. Furthermore, there is a need to know what happens to these products once they have reached the end of their useful life. This is especially true in the apparel industry where the current method of communicating the necessary information, the standard care

B. Iezzi, M. Shtein
Department of Materials Science and Engineering
University of Michigan
Ann Arbor, MI 48109, USA
E-mail: mshtein@umich.edu
A. Coon, L. Cantley, B. Perkins, E. Doran, T. Wang, M. Rothschild
MIT-Lincoln Laboratory
Lexington, MA 02421, USA

The ORCID identification number(s) for the author(s) of this article can be found under https://doi.org/10.1002/admt.202201099.

label, can be misleading or inadequate. A study of post-consumer clothing found that 29% did not have a legible care label; of those that did, 41% had inaccurate composition information.[1] Missing or inaccurate knowledge around fiber composition can make textile recycling, with rates currently less than 15% in the United States, cost-prohibitive; leading to over 17 million tons of textiles being sent to the landfill each year.[2,3] The Sorting for Circularity Project Europe, covering Belgium, Germany, the Netherlands, Poland, Spain, and the United Kingdom, recently estimated that, with efficient sorting infrastructure, it would be possible to profitably recycle 74% of current end-of-life fabrics, either mechanically or chemically, into fibers for new garments.[4] Thus, a more efficient sorting system of textiles for recycling or upcycling into high-value feedstocks is needed. A more accurate and durable labeling approach that also enables an automated, rapid sorting, and tracing system could dramatically increase recycling rates, detection of counterfeiting, and intellectual property or material theft.

Deficiencies in the standard care label have been known for decades, and many alternatives have been proposed and prototyped. In the early 2000s, radio frequency identification (RFID) clothing tags were introduced due to the ability to scan many tags from a distance simultaneously, and while gaining broader market reach in recent years, have not been implemented widely due to high cost and privacy concerns.[5,6] More recently, quick response (QR) codes have increased in popularity, as they enable each item to be assigned a unique code, and are readable with now-ubiquitous smartphones. A major drawback to QR codes, or any tag-based barcode, is that they are typically attached at the stage where the garment is manufactured from the constituent textile, thereby missing critical steps that preceed and follow in the textile supply chain, and thus falling short on the product life cycle and traceability requirements, as **Figure 1**A illustrates. Furthermore, they are easily detachable and/or become unreadable over the lifetime of the garment. Focused on creating non-removable tags, researchers also proposed using a randomized pattern of magnetic nanoparticles screen-printed onto a garment as a "secured" tag, as well as integrating a yarn segment that was colored and twisted in a particular manner to encode
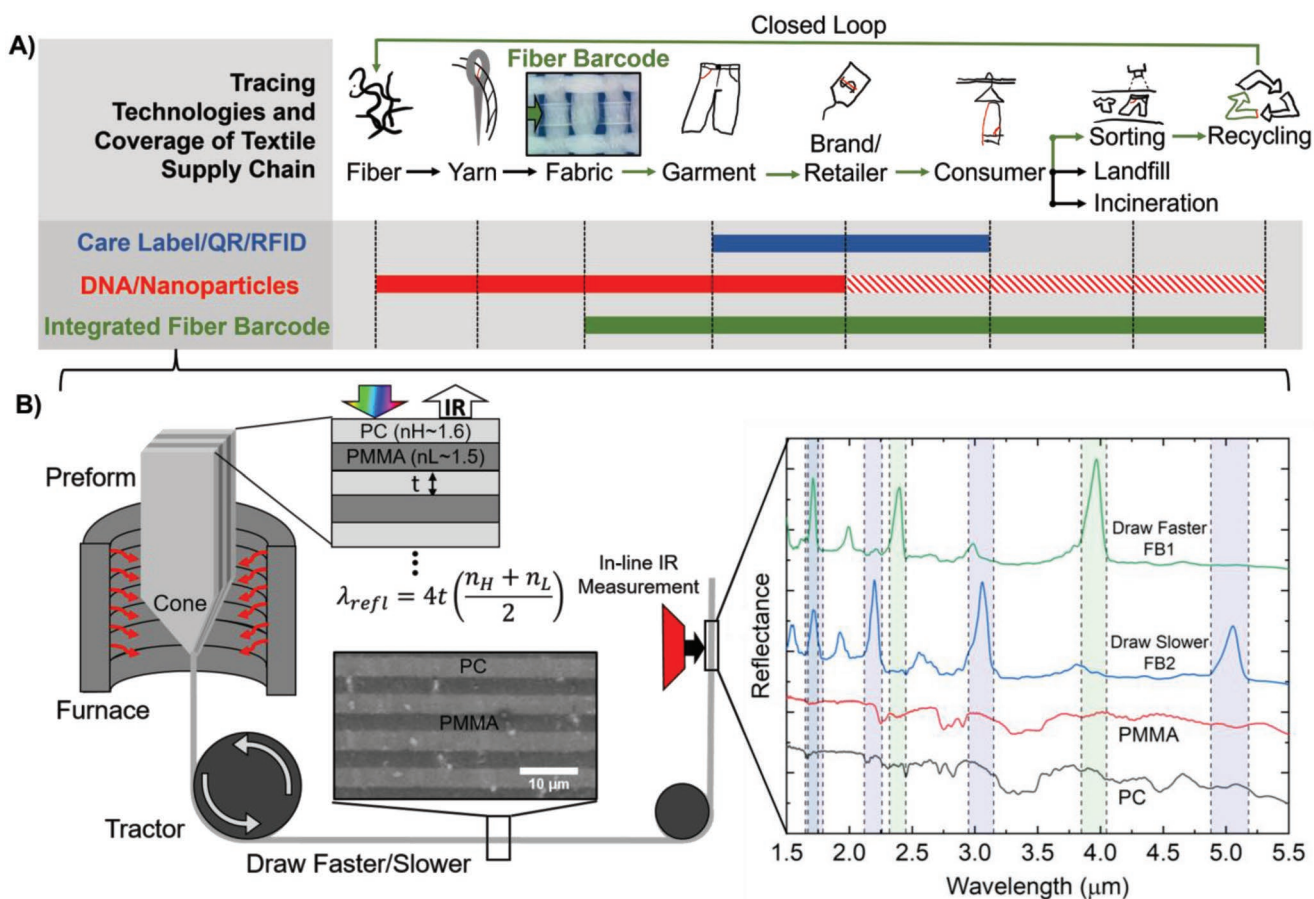
Figure 1. Tracing technology coverage of textile supply chain and proposed integrated fiber barcode (FB). A) The textile supply chain can be categorized into segments: fiber to yarn, to fabric, to garment, to retailer, to consumer, to end-of-life. Currently, end-of-life typically means being sent to the landfill but an alternative path is being developed in which end-of-life textiles go to a sorting facility and are then recycled. The standard care label, as well as QR codes and RFID tags (blue trace), are typically added at the garment stage and are typically removed/unreadable after consumer use. DNA and fluorescent nanoparticle tracing methods (red trace) can be integrated at the fiber stage but are not easily readable by consumers or at high speeds on commercial sorting equipment (patterned red trace). A fiber-based barcode is integrated directly into the fabric and can be read quickly at intermediate life cycle stages, as well as at automated sorting facilities (green trace) enabling a closed material loop. B) Schematic of photonic crystal fiber manufacturing by thermal drawing. A macroscale preform composed of alternating layers of commercially available polycarbonate (PC) and polymethyl methacrylate (PMMA) films are thermally drawn into a microscale fiber with sub-5 μm layer thicknesses (see SEM of fiber cross-section inset). Given the refractive index contrast between PC and PMMA ($\Delta n \approx 0.1$), a fiber with a desired infrared reflectance spectrum (λ_{refl}) is achieved through varying draw rates; higher rates result in thinner layers (*t*). In-line FTIR measurements are utilized to compare the infrared reflectance signatures of the photonic fibers to the inherent absorption in the constituent materials of the fiber (right plot).

information.[7,8] Both methods require complex algorithms to deconvolve and identify the patterns that have been created, whether on the fabric or in the yarn itself. More recent efforts to achieve early identification of fibers have utilized trace amounts of either customized DNA sequences or fluorescent nanoparticles to "tag" fibers directly.[9,10] While both methods are traceable throughout the life cycle, they have high laboratory testing costs (polymerase chain reaction detection for DNA) or direct material costs (rare earth fluorescent nanoparticles can cost >$30 mg^{-1}). Furthermore, the nanoparticles may be difficult to remove at the recycling stage and have the potential to contaminate the optical signal of future batches. No fiber or fabric-integrated tracing system has been developed yet that allows for low-cost, accurate, and high-speed identification at all life cycle stages.

Near-infrared (NIR) spectroscopy has seen considerable investment by municipalities in Europe to enable the identification and sorting of kilotons of post-consumer textiles for subsequent recycling, most notably the SipTex and FiberSort programs.[11] Polyester, cotton, silk, and wool all have different infrared "fingerprints"; molecular groups in the fibers absorb and reflect light differently, and thus, can be used to differentiate textiles based on fiber content.[12] Previous reports have shown, however, that identifying fiber blends from their NIR signatures is error-prone due to numerous and overlapping absorption peaks from the constituents, preventing quantification of the percentages of the overall composition, information critical for the recycling process.[13–15] Even more advanced optical techniques, such as hyperspectral imaging, had difficulty classifying fiber blends as well.[16]

**ADVANCED
SCIENCE NEWS**

www.advancedsciencenews.com

**ADVANCED
MATERIALS
TECHNOLOGIES**

www.advmattechnol.de

A potential solution to the challenges described above is to integrate an optical identifier into the fabric that is spectrally unique from the chemical absorption profile of the fabric constituents or contaminants, and can be cataloged and read like a barcode. It would enable not only chemical identification but also carry additional information downstream of the "yarn" stage in Figure 1A, such as the fiber source for the yarn and fabric manufacturing conditions. To enable such a "barcode," a strong, spectrally tuned, deterministically controlled reflectance response is needed to differentiate it from the background reflectance and absorption of the fabric.

One route to achieving a strong reflectance "fingerprint" is by creating a photonic crystal (PhC), which typically comprises periodic, quasi-periodic, and/or aperiodic arrangements of matter, each region having different refractive indexes and dimensions on the order of the wavelength of light meant to interact with the crystal. Photonic crystals in which the refractive index varies in only one dimension are known as 1D photonic crystals (1DPhCs). Controlling the composition and spatial arrangement leads to controllable optical signatures in reflection, absorption, and transmission. This high level of optical control has enabled the use of photonic crystals in wide-ranging applications including lasers and highly sensitive chemical sensors.[17,18] While typical photonic crystal designs rely on high index contrast materials, attained via inorganic dielectrics and semiconductors (e.g., titania, silica, and gallium arsenide alloys), there has been an increasing interest in utilizing purely organic dielectrics (polymers).[19] While typically having a lower index contrast than inorganic dielectrics, using polymers in 1DPhCs in principle enables high throughput cost-effective manufacturing, as well as customized prototyping using additive manufacturing methods.[20–22] The relatively low temperatures required for the thermal forming of polymers have allowed for high-throughput direct extrusion of 1DPhC fibers through customized spinnerets, relevant to fiber production.[23] Direct extrusion of photonic crystal fibers could potentially help achieve cost parity with more standard synthetic yarns, enabling widespread adoption.

In Figure 1B, we consider an implementation of a 1DPhC in the form of stacked polymer layers of different refractive indices. Furthermore, we consider the use of well-established thermal drawing as a method for size reduction of the laminated "preform" to achieve the desired length scale of refractive index domains.[24] By tuning the thickness and refractive index contrast between each layer, it is possible to create reflectors with a unique photonic response, where the final detection "fingerprint" is achieved after a geometric reduction of a macroscopic preform down to the microscale during thermal fiber drawing. In this work, fibers containing over 100 alternating layers of low refractive index contrast polymers enable the creation of both high-intensity and narrow (based on the full width at half maximum [FWHM]) reflectance peaks that can be tuned from the visible to the mid-infrared (0.5–16 µm). Furthermore, the fiber reflectance peaks are located away from typical regions of parasitic absorption. This enables the creation of kilometers of fiber with a precise, arbitrarily created photonic response that can be read using existing spectrophotometric methods that require a high signal-to-noise ratio versus background material absorption. The rest of this manuscript details the key production steps and associated photonic properties of the fibers, as well as demonstrates the behavior of the fiber in woven textiles.

2. Results and Discussion

For a given combination of refractive indexes of the two polymers inside the fiber, it is possible to alter the photonic response by changing the thickness of the layers via the rate at which the fiber is pulled, as shown in Figure 1B. Generally, higher draw speeds result in increased draw down ratios (DDR), or the geometric reduction of feature size in the final fiber as compared to the original preform. Increased DDRs result in thinner layers, blue-shifting the fundamental photonic response of the fiber (**Figure 2**A). Typically, a 1DPhC is designed for photonic peak response at a single fundamental wavelength, but in this work, the aim is to use a combination of the fundamental resonance with multiple overtone peaks, creating a barcode "fingerprint." Proper placement of the signature spectral features within the electromagnetic spectrum is critical, as parasitic absorption in the mid- and long-wave infrared (5.5–13.5 µm) would reduce signal strength, as is evident in the extinction coefficient plot in Figure 2A.

Designing for multiple overtone peaks in the 1.5–5.5 µm regime, where the extinction coefficient is less than 10^{-3}, increases reflectance. This is compared to peak extinction coefficient values of greater than 0.6 in the mid-IR. Importantly, the fundamental and overtone peaks discussed here are in relation to the peaks created by constructive and destructive interference induced by the refractive index contrast between layers, which here is ≈0.1, depending on wavelength. Resultant interference spectra can therefore be engineered and modified to encode desired information, not limited to only the material composition. This contrasts with fundamental and overtone absorption peaks that appear as integer multiples of certain functional groups in the organic molecules. This will be discussed further in Section 2.2, as it impacts measurement at shorter infrared wavelengths.

An important consideration for realizing multiple overtone peaks is the difference between even- and odd-ordered overtones. When the optical thickness (n_λ*layer thickness) of both materials is nearly equal, the even-order overtones destructively interfere. Given the relatively close refractive index of the two polymers and similar layer thicknesses, there are certain draw conditions, mainly when the lower index polymethyl methacrylate (PMMA) layers are thicker than the PC layers, where this destructive interference could occur and is demonstrated by the odd overtones in Figure 2A. When the material layer thicknesses shift away from the optical thickness, as in the simulation and experimental data from a drawn fiber in Figure 2B, both even and odd overtones are apparent. Factors that determine the spectral signature include layer thickness and refractive index contrast, as previously mentioned, as well as the number of layers in the photonic crystal. Increasing the number of layers results in a decrease in the peak FWHM, as well as an increase in reflectance (Figure 2C). This peak sharpening effect applies to both the fundamental peaks, as well as the overtones.
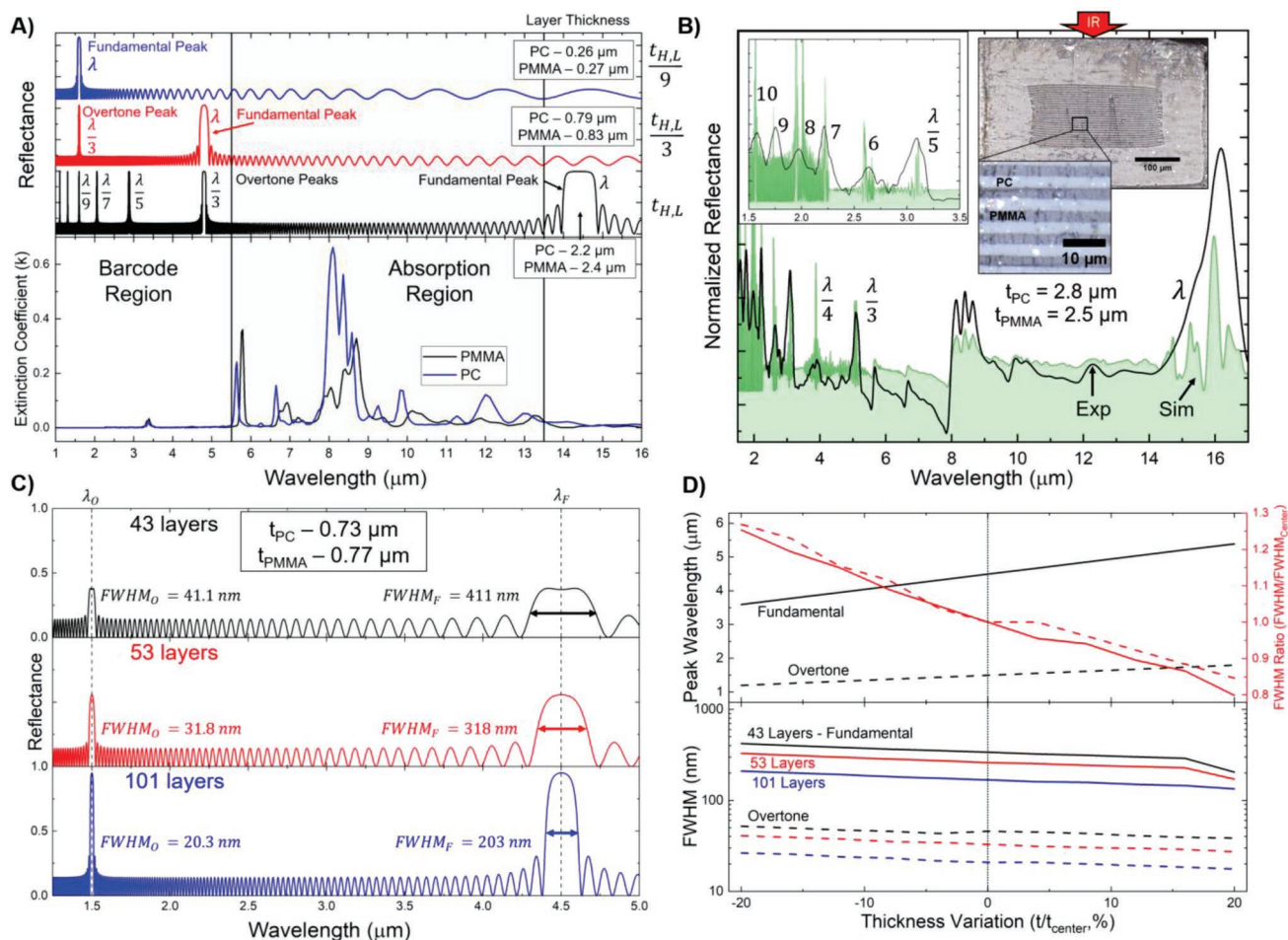
Figure 2. Fundamental and overtone peak utilization as barcode. A) The concept of a fiber with a "barcode" signature is achieved by creating multiple overtone peaks in the region from 1–5.5 µm. A general design framework for creating a certain number of overtone peaks in the barcode region is provided by modulating the thickness of the layers. The fundamental and overtone reflectance of a photonic crystal with high (t_H) and low (t_L) refractive index material layer thicknesses is shifted to shorter wavelengths by decreasing the layer thickness as indicated by the red ($t/3$) and blue ($t/9$) traces. The engineered fingerprint is derived from the location and shape of the prominent peaks as opposed to the typical FTIR fingerprint, which is derived from characteristic molecular absorption in the mid-infrared spectrum (5.5–13.5 µm, shaded). Peaks demonstrated are odd overtones as the optical thickness of the PC/PMMA bilayer ($n_{PC,PMMA}*t_{PC,PMMA}$) are almost equal leading to the cancellation of even-ordered overtones. B) Comparison of measured fiber infrared spectra (black trace) with transfer matrix simulations (green trace) derived from layer and cladding thicknesses. A micrograph of the fiber cross-section is included in the inset, showing how the optical thickness of the two layers is not equal, and the resultant even and odd overtone peaks. C) Transfer matrix simulations of the dependence of fundamental and overtone peak full width at half maximum (FWHM) and reflectance intensity on the number of layers in the photonic crystal. Reflectance intensity increases with increasing layer number while fundamental and overtone peak FWHM decreases with increasing layer number. D) During the fiber drawing process, variations in thickness can lead to shifts in the peak wavelength and FWHM (top, left axis). When thickness varies above or below a certain setpoint there will be a linear shift in the peak wavelength location. As layers become thicker, the FWHM of both fundamental and overtone peaks will decrease until the point where the structure is no longer resonant at that wavelength, signaling a shift to the next highest-order resonant peak (top, right axis). The number of layers in the photonic crystal is also a determining factor of FWHM, as more layers will result in narrower peaks for both fundamental and overtone resonances (bottom). The odd overtone ($\lambda/3$) has approximately an order of magnitude smaller FWHM than the fundamental.

The fiber draw process has inherent fluctuations that result in variations in the final fiber geometry, thus affecting the photonic response of the fiber. Transfer matrix simulations quantifying the photonic response due to fluctuations above and below a target thickness are provided in Figure 2D. There is a linear relationship between the peak wavelength and the layer thickness of the photonic crystal; a 5% shift in layer thickness results in a 5% shift in the peak wavelength. Furthermore, the ratio of FWHM at a certain thickness variation to the central FWHM decreases with an increasing variation. This holds until the point that the peak (whether fundamental or overtone) shifts to the next resonance order position. Finally, the FWHM of an overtone peak is narrower than that of a fundamental peak, depending on the number (i.e., $\lambda/2$, $\lambda/5$, etc.) of the overtone, with FWHM decreasing for higher-order overtones. Practically, a variety of signatures will be required to convey information about different brands and products, as well as coding for fiber composition and property information for recycling, such as intrinsic viscosity.[25] Previous work has shown 16 different combinations of polymers with differing refractive

indices can be drawn thermally, while the number of possibilities is likely larger given developments in polymer synthesis.[23] The number of layers is also a discrete parameter with anywhere from 50 to 100 layers providing the required reflectance intensity and narrow FWHM for measurement. Finally, layer thicknesses can be continuously tuned by adjusting the draw and feed rate, which will be discussed more in the next section. This results in a large number of potential combinations, excluding variations in the sequence of material layers (such as from n_L to n_H or n_H to n_L) and others, thus pointing to the utilization of these photonic signatures as unique product identifiers. In the next section, the experimental results of various drawn fibers are discussed.

2.1. Fabrication and Vis/IR Characterization of Multilayer 1DPhC Fibers

During the draw process, the volume of preform material entering the furnace and the volume of fiber material pulled from the cone within the furnace is conserved. Thus, as the draw speed is increased, the cross-section of the fiber decreases; **Figure 3**A. The DDR defines this volume conservation as the macroscale preform is drawn to a microscale fiber, given by Equation (1)

$$DDR = \sqrt{\frac{\dot{D}}{\dot{F}}} \tag{1}$$

where $\dot{D}$ is the draw rate of the fiber out of the cone and $\dot{F}$ is the feed rate of the preform into the furnace, both in meters per minute. The full derivation for the DDR can be found in Figure S1, Supporting Information. For the preforms in this work, when the fiber is drawn at rates ranging from 3 to 9.3 m min^{-1}, it was possible to achieve DDRs of 30–130, Figure 3B. Original film thicknesses of 75 and 125 μm shrunk to ≈0.75 to 1.25 μm, respectively, in the final fiber at a DDR of 100 (see electron micrographs in Figure 3A). Smaller overall layer thickness reduces the number of possible states where constructive interference can occur at a particular wavelength, and thus, the number of peaks for the given regime (e.g., 1.5–5.5 μm) decreases as well, Figure 3C. The colored traces on each plot correspond to transfer matrix simulations which take the average (green), maximum standard deviation (red), and minimum standard deviation (blue) of the PC and PMMA layer thicknesses as inputs including PC cladding thickness.

Even minor changes in layer thickness can result in a shift in the interference patterns, as previously discussed. The variation in layer thicknesses also helps explain the broad experimental peaks noted in several samples. This is most apparent in the sample drawn at 4.5 m min^{-1} where the peak at 5.1 μm is best fitted by a combination of the three simulations. There are also certain peaks that appear in the experimental data but are not predicted by simulation, such as the peak at 2.7 μm for the 5.5 m min^{-1} fiber. This may be partially due to absorption in the PC cladding; simulations show peak intensity increases with a reduction in cladding thickness. In an industrial environment, if a certain barcode response must be achieved and maintained, the DDR based on draw rate and feed rate becomes a critical

control parameter. The fiber draw tower used in this study has in situ infrared measurement capability, and the results from those measurements are shown in Figure 3D. Peak shift to shorter wavelengths at higher draw rates, and thus thinner layers, is demonstrated and is correlated to the DDR. Note the "dark" region at ≈3.4 μm, due to increased molecular absorption at this wavelength in both the PC and PMMA (Figure 2A).

To explore the tunability of the photonic response, a fiber was created that had twice the number of layers (101 layers) that were individually thinner (75 vs 125 μm) in the preform. Generally, increasing the number of layers in a 1DPhC increases reflectance intensity for a fixed refractive index contrast. The peak reflectance depending on the number of layer pairs (N) is approximately given by Equation (2)[26]

$$R \cong \left(\frac{n_0 (n_H)^{2N} - n_S (n_L)^{2N}}{n_0 (n_H)^{2N} + n_S (n_L)^{2N}} \right)^2 \tag{2}$$

where n_0 is the refractive index of air and n_S is the refractive index of the substrate. Since measurements are made with a polycarbonate (PC) cladding as a backing to the photonic crystal insert within the fiber, the same refractive index is used for n_H and n_S. Furthermore, the minimum FWHM for the layer pair of PC and PMMA is approximately given by Equation (3)[27]

$$FWHM \cong \frac{4\lambda_0}{\pi} asin \left(\frac{n_H - n_L}{n_H + n_L} \right) \tag{3}$$

These analytical solutions are compared to numerical simulation results in Figure S2, Supporting Information, and show good agreement. The results of the experiment with the 101-layer fiber are shown in **Figure 4**. Using thinner layers in the preform resulted in sub-micrometer layer thicknesses in the drawn fiber, exhibiting fundamental reflectance peaks in the 1.5–5.5 μm regime at DDRs of 92, 110, and 126 in Figure 4C. The in situ photonic data in Figure 4D shows similar behavior to the 53-layer fiber, in that higher DDRs (i.e., more and thinner layers) resulted in a blue shift.

The peak reflectance intensity, measured via μ-FTIR, of the 53-layer fiber drawn at 7.5 m min^{-1} was 19% while the 101-layer fiber drawn at 5 m min^{-1} was 51%, demonstrating how an increased number of layers increases reflectance. In addition to providing higher reflectance intensity, an increase in layers also increases the sharpness of the peaks, measured by their FWHM. The 53-layer fiber drawn at 7.5 m min^{-1} and the 101-layer fiber drawn at 5 m min^{-1} are compared due to their similar layer thicknesses and overtone peak locations. The FWHM of the first overtone ($\lambda/2$) for the 53-layer fiber is 170 nm while the 101-layer fiber is 139 nm, as was predicted in Figure 2C. However, the second overtone ($\lambda/3$) for the 53-layer fiber is lower (75 nm) than the 101-layer fiber (103 nm). The simulated FWHM for the second overtone for the 53-layer fiber is 12.6 nm while for the 101-layer fiber it is 14.4 nm, like what was seen experimentally. While the experimental peak FWHM is nearly an order of magnitude larger, likely due to imperfections induced during the manufacturing process, the simulated FWHM helps predict trends depending on the number of layers. Further peak FWHM analysis is summarized in Figure S3, Supporting Information.

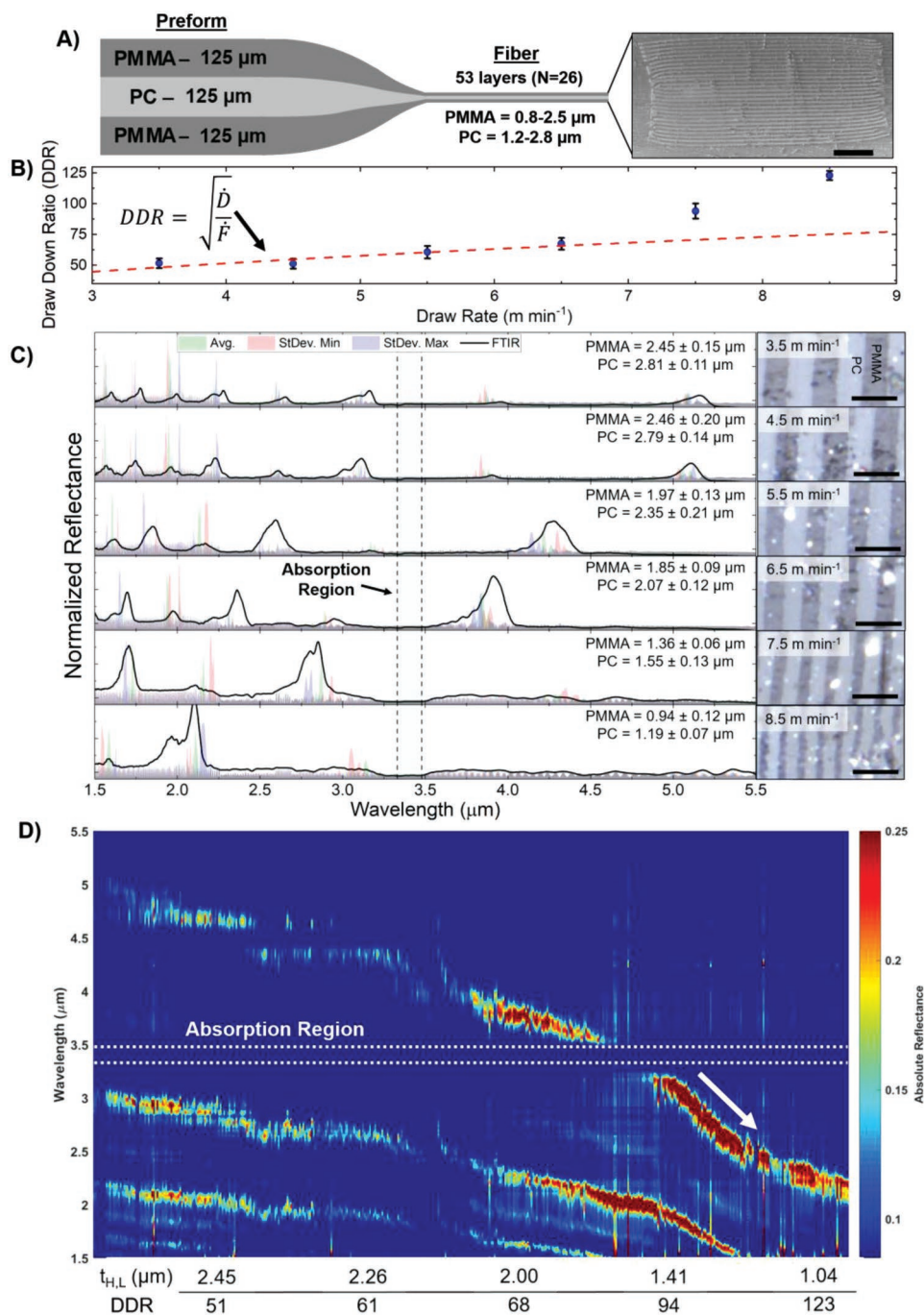**Figure 3.** Photonic response of PMMA/PC fiber with 53 layers. A) Original preform consists of 53 alternating layers (or 26-layer pairs, *N*) of PMMA and PC films that are 125 μm thick along with resultant SEM micrograph (scale bar 50 μm) of fiber drawn at 3.5 m min⁻¹. B) Comparison of the model of draw down ratio (DDR) and measured DDR at different draw rates. Model holds for lower draw rates but increases quickly above 7 m min⁻¹. C) Static spectral reflectance measured via FTIR microscopy of 53-layer fibers drawn at increasing rates, resulting in increasing draw down ratios and thinning of polymer layers. Optical micrographs provided show increased relative thinning of PMMA layers as compared to PC layers (scale bar for all 5 μm). Layer thicknesses (average, maximum standard deviation, minimum standard deviation) were utilized in a transfer matrix model to obtain simulated reflectance spectra (green, red, and blue-filled traces). D) Results of in situ FTIR microscopic measurements showing a blue shift in peak wavelength location with increasing DDR (and decreasing layer thickness). Increase in DDR is noted by the white arrow.

Using alternative polymers with different refractive indices will also modify the FWHM and absolute reflectance. For example, if a lower refractive index thermoplastic polymer, such as polytetrafluoroethylene (PTFE, *n* ≈1.32) was utilized in place of PMMA in the 1DPhC stack, the FWHM of the second overtone would, theoretically, increase nearly threefold (Figure S4,

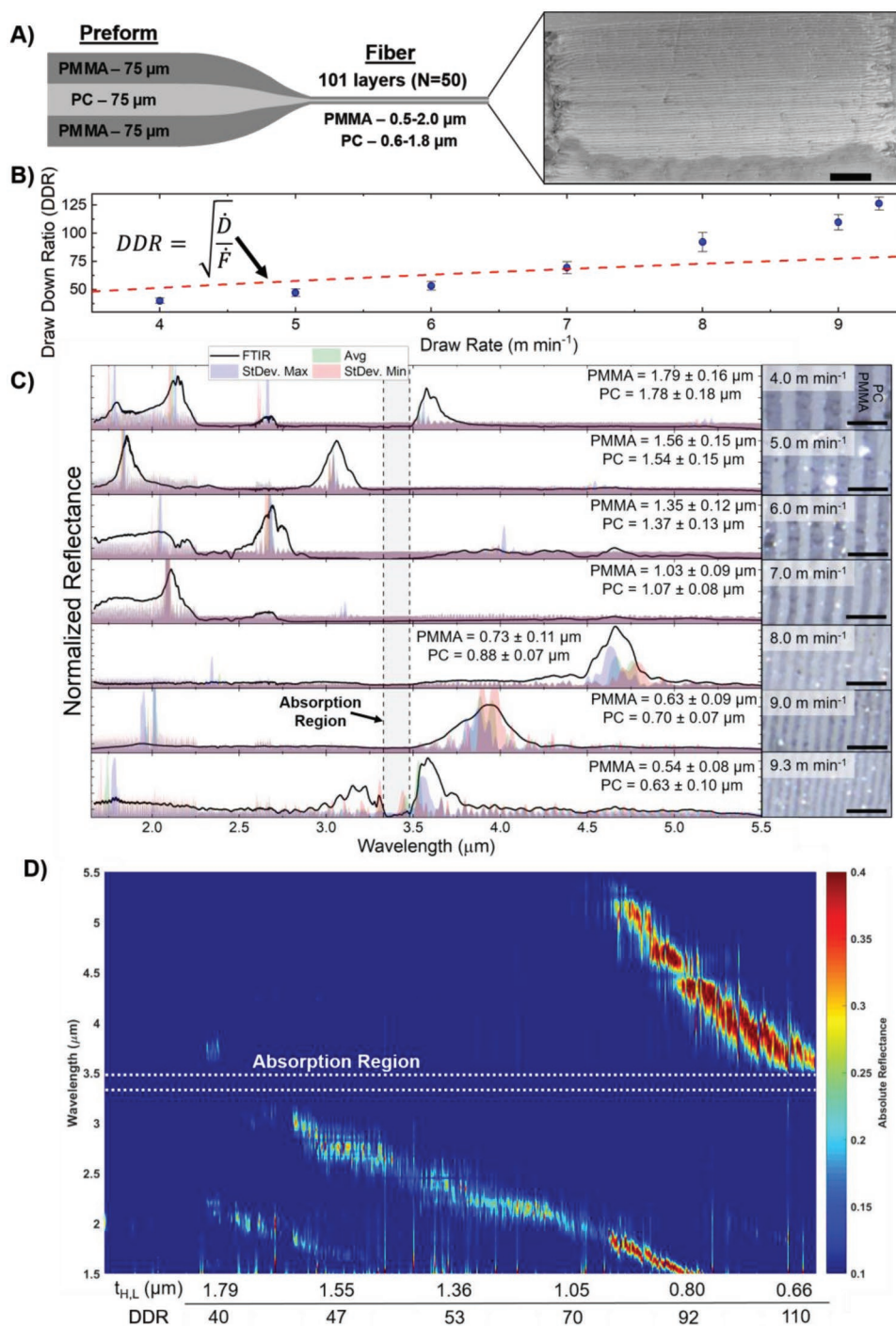**Figure 4.** Photonic response of PMMA/PC fiber with 101 layers. A) Original preform consists of 101 alternating layers (or 50-layer pairs, *N*) of PMMA and PC films that are 75 μm thick each. A resultant SEM micrograph (scale bar 50 μm) of fiber drawn at 4 m min⁻¹ is also provided. B) Comparison of model of draw down ratio (DDR) and measured DDR at different draw rates. Model holds for lower draw rates, but like Figure 3, increases quickly above 7 m min⁻¹. C) Static spectral reflectance measured via FTIR microscopy of 101-layer fibers drawn at increasing rates, resulting in increasing draw down ratios and thinning of polymer layers. Optical micrographs provided show increased relative thinning of PMMA layers as compared to PC layers (scale bar for all 5 μm). Layer thicknesses were utilized in a transfer matrix model to obtain simulated reflectance spectra (blue/green/red filled traces) which show good agreement with measured spectra. The molecular absorption of PMMA and PC around 3.4 μm can be seen clearly in the 9.3 m min⁻¹ sample with a peak split occurring. D) Results of in situ FTIR microscopically resolved measurements showing a blue shift in peak wavelength location with increasing draw rate (and decreasing layer thickness).

Supporting Information). This is important to consider for future development, as similar peak broadening in a higher refractive index contrast material pair may cause neighboring overtone peaks to overlap, and thus, degrade the fidelity of the barcode signature.

Note that the reflectance response in a 1DPhC typically depends on the angle of incidence (AOI) of the probe beam. Understanding the angle-dependent behavior is important, as the scanning system of the fiber barcode must be able to identify a specific signature at off-normal incidence. Snell's Law (Equation (2))

$$\sin \theta_i = n_L \sin \theta_L = n_H \sin \theta_H \tag{4}$$

where θ_i is the AOI of light (assuming coming from the air where $n \approx 1$), can be modified to calculate the peak response wavelength of a 1DPC with AOI[28]

$$\lambda_C = \lambda_0 \left[(1 - \sin^2 \theta_i / n_L^2)^{\frac{1}{2}} + (1 - \sin^2 \theta_i / n_H^2)^{\frac{1}{2}} \right] \tag{5}$$

where λ_C is the center wavelength at that angle while λ_0 is the center wavelength at normal incidence (0°). The peak shift predicted by Equation (3), along with a diagram detailing the

experimental setup used to test it, is given in **Figure 5**A. The theoretical prediction matches well with the simulations conducted in Figure 5B, showing the predicted response of two different fibers that have a single peak in the 3–5 μm range (101-layer fiber at 9 m min⁻¹), as well as multiple peaks in the 1.5–5 μm range (53-layer fiber at 5.5 m min⁻¹). Experimental spectra collected at 10°, 12°–24°, 30°, 40°, 50°, 60°, and 70° AOI to the fiber show good agreement with the simulated predictions, allowing to compensate for the angle-dependent shift. We note also that the intensity of reflected light decreases at higher AOI, lowering the signal-to-noise ratio. However, a benefit of having multiple overtone reflectance peaks is that the wavelength location of the peaks will shift at the same rate, as shown in Figure 5C, and thus, the wavelength difference between two overtone peaks can also be utilized as an angle-independent identification marker. Furthermore, implementing a circular cross-section design for the photonic crystal layers could further reduce the angle dependence.

2.2. Optical System Analysis for Fiber Detection

Another key consideration for the widespread implementation and adoption of a photonic barcoding system is the ability to
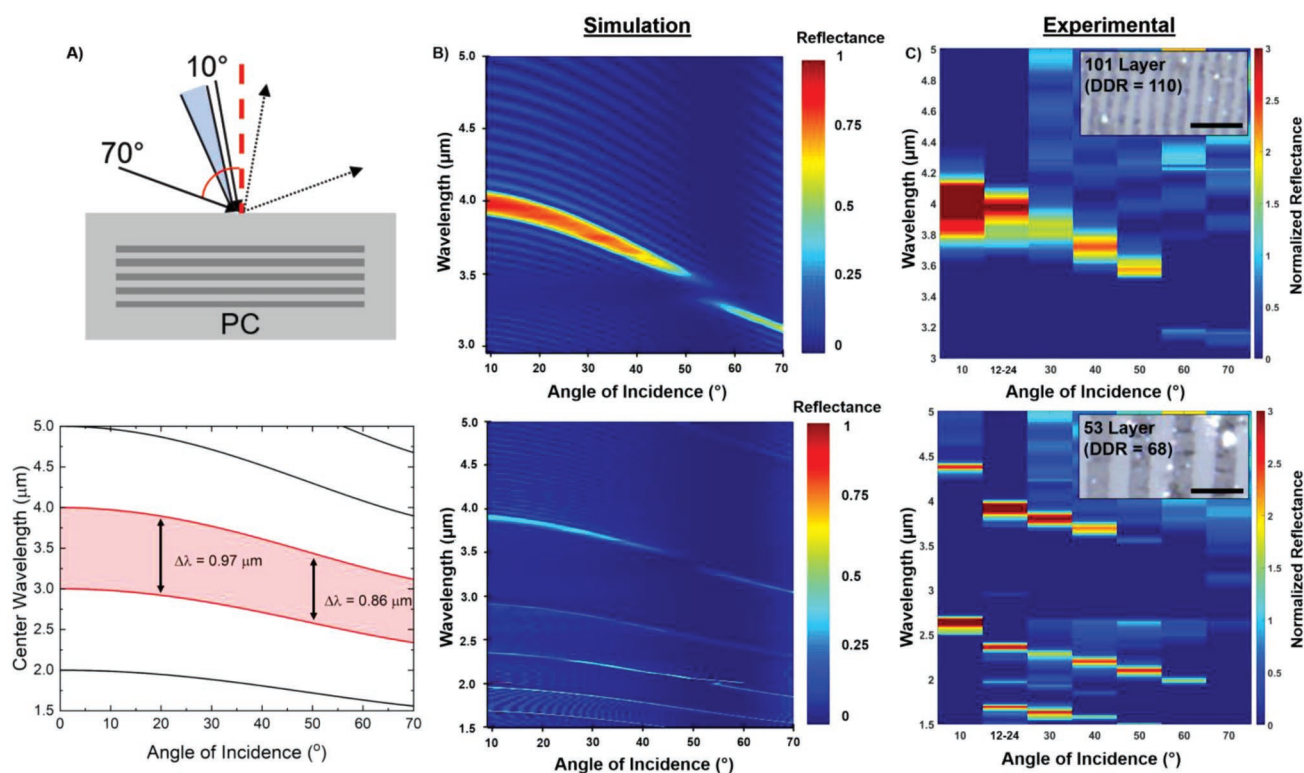

Figure 5. Dependence of photonic response on angle of incidence. A) Schematic of simulations and measurements of angle dependence on photonic response. A range is given for 12°–24° as this is the range of angles that the Cassegrain objective accepts that is used in the microscopic FTIR system. The bottom plot shows the result of Equation (3) plotted versus angle of incidence for multiple central wavelengths. The peak-to-peak distance decreases at higher angles. B) Top – angle-dependent transfer matrix simulations of 101-layer fiber (DDR = 110 from Figure 4) from 10°–70° showing an expected blue shift in the reflectance peak with increasing angle of incidence. Bottom – angle-dependent transfer matrix simulations of 53-layer fiber (DDR = 68 from Figure 3) showing that multiple peaks will maintain similar peak-to-peak distances regardless of the angle of incidence. C) FTIR spectra of the same fibers measured using a Pike 10Spec (10°), standard Cassegrain objective (12°–24°), and Pike VeeMax (30°–70°) systems showing good agreement with simulated fiber photonic response.
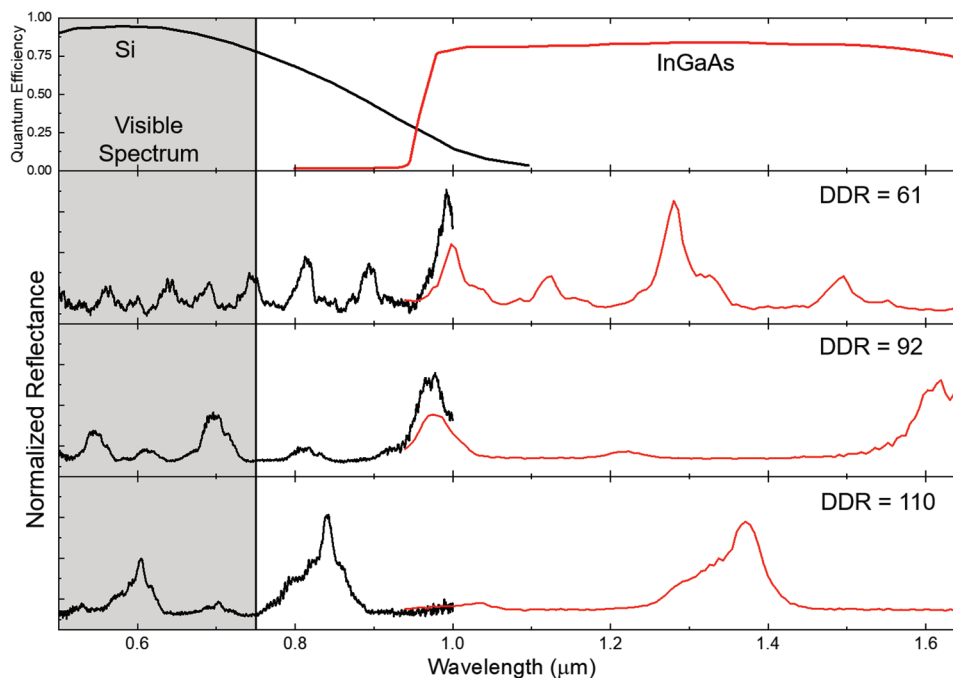
Figure 6. Visible and near-infrared (NIR) response of photonic fibers. Top: quantum efficiency of silicon (Si) and indium gallium arsenide (InGaAs) detectors versus wavelength. The visible spectrum (≈0.4–0.75 µm) is shaded for comparison. Bottom: visible and NIR response of three fibers drawn at different speeds (53-layer/DDR – 61, 101-layer/DDR = 92 and 110, respectively). All three fibers have multiple spectral peaks that are detectable in the visible wavelength regime. The black traces were collected using a UV/vis spectrometer while the red traces were collected using a NIR spectrometer.

read the spectral signature within the fiber, and ultimately the fabric, at a low cost. The cost of detection is directly related to which photodetection mechanism is used. The most widely used materials in industrial FTIR sensors are semiconductor alloys of mercury cadmium telluride (MCT or HgCdTe), which has high quantum efficiency (QE) from the near to far infrared. MCT detectors, however, require cryogenic cooling (typically liquid nitrogen), are relatively expensive to fabricate and are not widely used in field applications. In the NIR (0.75–1.65 µm), there are a wider array of materials that have good QE with the most common being indium gallium arsenide (InGaAs).[29] While also being expensive due to challenges in manufacturing, InGaAs detectors have the benefit of only needing thermoelectric cooling without the need for liquid nitrogen. Shifting to even shorter wavelengths, most cameras in commercial applications use silicon (Si) detectors, with high sensitivity in the range of 0.35–1.1 µm, no cooling requirements, and wide availability and very low cost. A comparison of the QE of Si and InGaAs, along with the reflectance of three different fibers in the visible and NIR (0.5–1.65 µm), is provided in **Figure 6**. All the fibers exhibit multiple spectral peaks present across this entire wavelength range, demonstrating that the barcode signature could be detected even using lower-cost spectrometers; NIR spectrometers directly integrated into a smartphone have been demonstrated.[30] The overlap of engineered reflectance spectra with pigments and dyes in colored fabrics is of potential concern, but can be mitigated by increasing the reflectance intensity of more layers or targeting the NIR detection window (0.75–1 µm) of silicon. While several of the fibers demonstrate narrowband reflectance in the visible wavelength range, it is important to note that the fibers themselves are typically transparent or translucent under ambient light, as shown in Figure S5, Supporting Information. This aids in eventual fabric integration without need for altering its appearance.

Another consideration for the overall measurement system is the availability of cost-effective light sources for the interrogation of textiles. While the exact details of the lamps and spectrometers utilized in commercial automated sorting systems are proprietary, some assumptions can be made. For example, handheld systems will most likely utilize either a visible or NIR light-emitting diode or a tungsten-halogen bulb. Larger, automated systems likely utilize larger tungsten lamps or potentially laser illuminators. Generally, the light sources are cheaper than the spectrometers, but if longer wavelengths (i.e., >2 µm) are needed for measurement, the cost of light sources increases compared to visible wavelengths.

2.3. Integration of Photonic Fibers into Woven Textiles

A key consideration for the widespread adoption of these photonic fibers as a barcoding system is the ability to be integrated with existing textile manufacturing processes. Weaving the photonic fibers into a background fabric was first attempted as the relatively flat weave enables easier spectroscopic measurement. In **Figure 7**A, an optical microscope image is given of the photonic crystal fiber being integrated into a plain weave polyethylene (PE) fabric. The fiber is effectively transparent in the visible regime, which lends itself to being an aesthetically neutral addition to a garment. The concept of weaving a certain amount of fiber into a pair of pants is also shown and then how the garment might be measured on an automated infrared sorting system.
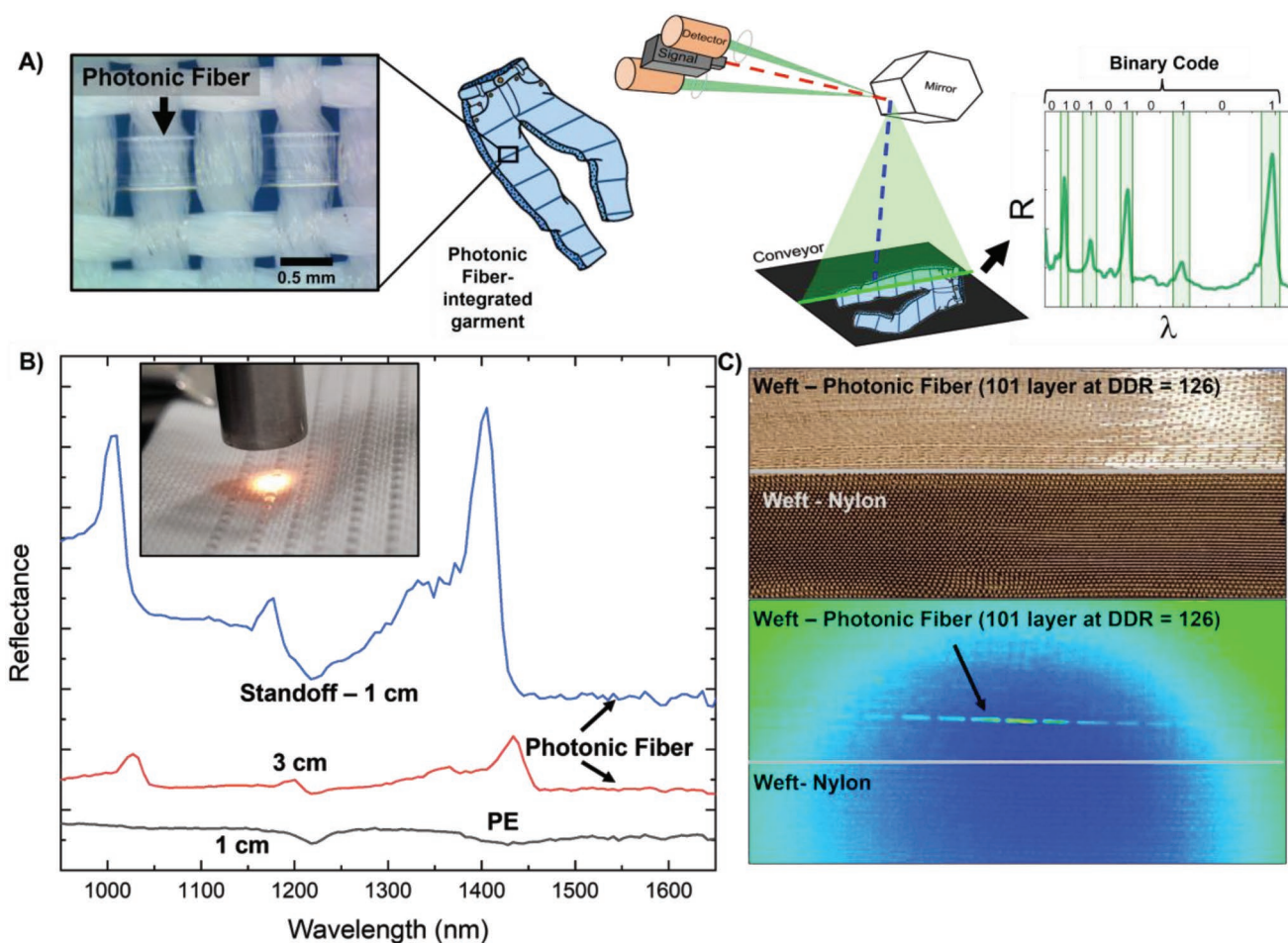
**ADVANCED
SCIENCE NEWS**

www.advancedsciencenews.com

**ADVANCED
MATERIALS
TECHNOLOGIES**

www.advmattechnol.de

Figure 7. Spectral response of photonic fiber-integrated fabrics. A) Optical microscope image of photonic fiber integrated into a plain weave with polyethylene (white fibers). A schematic is given that shows how the photonic fiber could be integrated at the garment level for tracking and sorting by commercial-scale near-infrared spectral sorting systems. Peaks with a certain center wavelength and FWHM will be associated with a specific code based on the peak/valley sequence. B) Near-infrared spectral response of the photonic fiber that has been integrated into the same polyethylene fabric as 5A. Note that reflectance signal depends on the standoff height of the probe from the fabric. C) Polypropylene warp fabric with a satin weave of the photonic fiber in comparison to a nylon filler fiber (top) under visual illumination. The photonic fiber is transparent under visible illumination. In the lower panel, a short-wave infrared (1–5 μm) imaging camera is used to image the photonic fiber to the nylon. The photonic fiber has a much higher intensity than the nylon fiber and an individual photonic fiber (yellow dashed line in image) is demonstrated. This image was taken using a bandpass filter with a center wavelength of 3.5 μm.

The proposed identification system would associate the key spectral peak characteristics with a database that contains previously recorded spectral signatures, categorized according to, e.g., the number of peaks, their location, and FWHM.

In Figure 7B, the inset image shows what the fiber looks like integrated into the woven fabric, as well as the measurement system used for measuring the NIR spectral response. The measured response of the photonic fiber is clearly apparent over that of the PE warp yarns. This difference also helps elucidate how different organic fibers are characterized in commercial systems. In the plot, there is a slight dip in reflectance of the PE fiber at ≈1.22 μm. In this case, this dip could correspond to the C–H stretch, which has a fundamental peak between 5.95 and 6.10 μm and is an approximate integer multiple of the overtone peak at 1.22 μm (5n). While these absorption overtones, based on fiber composition, are currently used to identify fiber content, they are orders of magnitude lower in intensity

than the fundamental absorption which occurs at longer wavelengths.[31] The ability to differentiate the photonic fiber from the background textile was further explored using short-wave infrared (SWIR) imaging with a response from 1 to 5 μm (Figure 7C). A nylon fiber was added as a weft yarn and woven next to the photonic fiber; a photonic filter was chosen with the same spectral window where the fiber is expected to have a reflectance peak, here at 3.5 μm. A comparison of the spectral window overlap with the fiber is summarized in Figure S6, Supporting Information. The photonic fiber is clearly visible in yellow while the nylon fiber does not appear in sharp contrast. Note that the rest of the photonic fibers do not appear as bright, likely due to the filter being of smaller physical size than the lens of the camera, resulting in a vignetting effect. The fibers with higher DDR (generally >80) were more easily woven into fabrics due to similar cross-sectional dimensions to the other warp and weft yarns. These results show that the photonic fiber

can be integrated with industrially relevant processes and is a clear marker in the finished fabric.

3. Conclusions

We demonstrated a novel approach to creating all-polymer photonic crystals within textile-compatible fibers. The resultant visible, near-, and mid-infrared reflectance response of those fibers was characterized under different manufacturing conditions. The spectral response was shown to depend on the draw conditions, mainly the speed at which the fiber is drawn, dictating the thickness of the high and low refractive index layers. The response of the fibers at various incident angles of light was also characterized, showing agreement with numerical predictions. The novel, all-polymer, photonic crystal fibers were integrated into textiles and the resultant spectral response was demonstrated to be clearly observable against the background textile, both via a single-point probe and a wide field-of-view imager. Overall, this approach, including fiber configuration, production, integration, and characterization, was shown to have strong potential for integration into industrially-relevant manufacturing processes to enable enhanced tracing and sorting of textiles for product life cycle management.

4. Experimental Section

Preform Materials and Drawing Conditions: Photonic crystal fiber preforms were fabricated by placing a multilayer stack of PMMA ($n \approx 1.5$) and PC ($n \approx 1.6$) films into the center of a milled PC bar and then covered with an additional PC bar to protect the photonic crystal insert. The films were commercially sourced (Roehm – PMMA and Tekra – PC) and had thicknesses of either 75 (3 mil) or 125 µm (5 mil). The preforms were typically 300–350 mm in length with a 16 mm by 26 mm cross-section. Preforms were consolidated using a Grimco hydraulic press at 200 kg of force and a top and bottom platen temperature of 175 °C. An Advantek Engineering custom draw tower with a three-zone furnace was used to heat the preform and initiate the draw process. For all fibers presented in this work, the following zone temperatures were used: the top zone set to 150 °C, the middle zone set to 270 °C, and the lower zone set to 110 °C. The feed rate of the preform into the furnace was kept constant at 1.5 mm min^{-1}. Once the draw process was initiated, the drawn cross-section size of the fiber was controlled by altering the tractor speed on the tower. Tractor speeds from 3 to 9.3 m min^{-1} were utilized which resulted in DDRs of around 30–130 times, with higher speeds resulting in higher DDRs. The DDR was calculated as the initial cross-section geometry divided by the final cross-section geometry. Drawn fiber samples were cross-sectioned and polished for microscopy analysis utilizing a scanning electron microscope (SEM), as well as a laser scanning microscope (Olympus LEXT).

Fiber Spectroscopic Characterization: Multiple spectroscopic systems were utilized for fiber photonic analysis. During the draw process, a customized feeding system was utilized with a Bruker Hyperion 2000 FTIR microscope equipped with a 15× Cassegrain reflective objective to collect in situ infrared reflectance measurements. The same microscope was also utilized for collecting static infrared measurements of the fibers. The Cassegrain objective had an actual measurement angle that averages between 12° and 24°. All fibers were measured with the longer axis of the cross-section normal to the microscope, which oriented the photonic crystal normal to the measurement axis. Angled fiber measurements were made utilizing PIKE Technologies VeeMax (30°–70°) and 10Spec (10°) reflective adapters that were placed in the bench compartment of the Bruker Vertex 70 FTIR. Multiple fibers

were placed parallel to each other to cover the 10 mm aperture of the adapters. NIR spectroscopic measurements were made with a system composed of a Thorlabs SLS202L broadband light source (0.45–5.5 µm) that was coupled to an Ocean Insight Vis/NIR reflectance probe (R400-7-VIS-NIR) and a FLAME NIR spectrometer (0.95–1.65 µm). For visible spectroscopic measurements, the same light source and reflectance probe were utilized but the spectrometer was switched to an Ocean Insight HR2000+ spectrometer (0.2–1.1 µm). All infrared measurements were made with reference to a specular gold mirror while the visible measurements were made with reference to a specular aluminum mirror. All simulations were conducted using the STACK solver of Lumerical FDTD with wavelength-dependent refractive index and extinction coefficient data for PC and PMMA taken from the literature.[32,33]

Weaving Parameters and Short Wave-Infrared Imaging: All woven samples were fabricated on a rapier loom (CCI Studio Loom) capable of making fabrics 508 mm wide. All photonic fibers were integrated as weft yarns with the warp being composed of either a 370 decitex high-density polyethylene yarn with 300 twists per meter "z" twist at 16 ends per cm or 220 decitex polypropylene yarn that was false twisted. Various weave patterns were also tested. The NIR fabric analyzed was composed of a 53-layer fiber drawn at 5 m min^{-1} integrated as a plain weave every fourth pick (16 picks per cm) with the HDPE warp using an 8-harness float. The fabric for short wave infrared imaging was based on a 101-layer fiber drawn at 9.3 m min^{-1} and a black nylon filler yarn integrated as a satin weave (also 8-harness float) with every pick (16 picks per cm). Short wave infrared imaging was conducted using a FLIR x6900sc camera (InSb detector) with illumination from a broadband tungsten lamp. An infrared bandpass filter (Thorlabs FB3500-500) centered at 3.5 µm with a 0.5 µm FWHM was utilized to obtain the spectral image in Figure 7C.

Supporting Information

Supporting Information is available from the Wiley Online Library or from the author.

Conflict of Interest

The authors declare no conflict of interest.

Data Availability Statement

The data that support the findings of this study are available from the corresponding author upon reasonable request.

[1] J. Wilting, H. van Duijn, Clothing labels: Accurate or not?, https://www.circle-economy.com/resources/clothing-labels-accurate-or-not (accessed: November 2021).

[2] P. Harmsen, M. Scheffer, H. Bos, *Sustainability* **2021**, *13*, 9714.

[3] United States Environmental Protection Agency – Office of Land and Emergency Management, Advancing sustainable materials management: 2018 fact sheet, https://www.epa.gov/sites/default/files/2021-01/documents/2018_ff_fact_sheet_dec_2020_fnl_508.pdf (accessed: December 2021).

[4] H. van Duijn, N. Carrone, O. Bakowska, Q. Huang, M. Akerboom, K. Rademan, D. Vellanki, Sorting for circularity Europe: An evaluation and commercial assessment of textiles waste across Europe, https://reports.fashionforgood.com/report/sorting-for-circularity-europe/ (accessed: November 2022).

[5] A. Juels, *IEEE J. Sel. Areas Commun.* **2006**, *24*, 381.

[6] R. Nayak, A. Singh, R. Padhye, L. Wang, *Fash. Text.* **2015**, *2*, 9.

[7] T. K. Agrawal, L. Koehl, C. Campagne, *Int. J. Adv. Des. Manuf. Technol.* **2018**, *99*, 2563.

[8] K. Wang, V. Kumar, X. Zeng, L. Koehl, X. Tao, Y. Chen, *Int. J. Comput. Intell. Syst.* **2019**, *12*, 713.

[9] A. P. Tran, A. Berrada, M. B. Liang, L. Jung, (APDN BVI Inc.), US 10760182B2, **2020**.

[10] M. Greene, P. Stenning, (Fibremark Solutions Ltd), US10247667B2, **2019**.

[11] M. Elander, Automated feeding equipment for textile waste: Experiences from the FITS project, http://mistrafuturefashion.com/wp-content/uploads/2019/10/M-Elander.-Automated-feeding-equipment-for-textile-waste.-Mistra-Future-Fashion-report.pdf (accessed: December 2021).

[12] P. Peets, K. Kaupmees, S. Vahur, I. Leito, *Herit. Sci.* **2019**, *7*, 93.

[13] T. L. Wong, U. K. Ahmad, S. Tharmalingam, *Probl. Forensic Sci.* **2015**, *103*, 163.

[14] K. Cura, N. Rintala, T. Kamppuri, E. Saarimäki, P. Heikkilä, *Recycling* **2021**, *6*, 11.

[15] W. Li, Z. Wei, Z. Liu, Y. Du, J. Zheng, H. Wang, S. Zhang, *Text. Res. J.* **2021**, *91*, 2459.

[16] C. Blanch-Perez-del-Notario, W. Saeys, A. Lambrechts, *J. Spectr. Imaging* **2019**, *8*, a17.

[17] K. Iga, *Jpn. J. Appl. Phys.* **2008**, *47*, 1.

[18] P. Lova, G. Manfredi, L. Boarino, A. Comite, M. Laus, M. Patrini, F. Marabelli, C. Soci, D. Comoretto, *ACS Photonics* **2015**, *2*, 537.

[19] P. Lova, G. Manfredi, D. Comoretto, *Adv. Opt. Mater.* **2018**, *6*, 1800730.

[20] G. Manfredi, P. Lova, F. Di Stasio, R. Krahne, D. Comoretto, *ACS Photonics* **2017**, *4*, 1761.

[21] K. D. Singer, T. Kazmierczak, J. Lott, H. Song, Y. Wu, J. Andrews, E. Baer, A. Hiltner, C. Weder, *Opt. Express* **2008**, *16*, 10358.

[22] B. Iezzi, Z. Afkhami, S. Sanvordenker, D. Hoelzle, K. Barton, M. Shtein, *Adv. Mater. Technol.* **2020**, *5*, 2000431.

[23] M. Asano, T. Kuroda, S. Shimizu, A. Sakihara, K. Kumuzawa, H. Tabata, (Nissan Motor Co., Ltd., Tanaka Kikinzoku Kogyo K.K., Teijin Limited), US 6,326,094 B1, **2001**.

[24] K. Stoeffler, C. Dubois, A. Ajji, N. Guo, F. Boismenu, M. Skorobogatiy, *Polym. Eng. Sci.* **2010**, *50*, 1122.

[25] J. C. Tapia-Picazo, J. G. Luna-Bárcenas, A. García-Chávez, R. Gonzalez-Nuñez, A. Bonilla-Petriciolet, A. Alvarez-Castillo, *Fibers Polym.* **2014**, *15*, 547.

[26] C. J. R. Sheppard, *Appl. Opt.* **1995**, *4*, 665.

[27] L. R. Brovelli, U. Keller, *Opt. Commun.* **1995**, *116*, 343.

[28] W. H. Southwell, *Appl. Opt.* **1999**, *38*, 5464.

[29] A. Ciocia, A. Carullo, P. Di Leo, G. Malgaroli, F. Spertino, in *2019 IEEE 46th Photovoltaic Specialists Conf. (PVSC)*, IEEE, Piscataway, NJ **2019**, 2734.

[30] V. Wiedemair, D. Langore, R. Garsleitner, K. Dillinger, C. Huck, *Molecules* **2019**, *24*, 428.

[31] J. Coates, *Appl. Spectrosc. Rev.* **1998**, *33*, 267.

[32] X. Zhang, J. Qiu, X. Li, J. Zhao, L. Liu, *Appl. Opt.* **2020**, *59*, 2337.

[33] X. Zhang, J. Qiu, J. Zhao, X. Li, L. Liu, *J. Quant. Spectrosc. Radiat. Transfer* **2020**, *252*, 107063.

2201099 (12 of 12)